Control Engineering Practice 148 (2024) 105949

Contents lists available at ScienceDirect

Control Engineering Practice

journal homepage: www.elsevier.com/locate/conengprac

Data-based modelling of arrays of wave energy systems: Experimental tests, models, and validation

Edoardo Pasta [a,*], Guglielmo Papini [a], Yerai Peña-Sanchez [b], Facundo D. Mosquera [c], Francesco Ferri [d], Nicolás Faedo [a]

[a] Marine Offshore Renewable Energy Lab., Department of Mechanical and Aerospace Engineering (DIMEAS), Politecnico di Torino, 10129, Corso Duca degli Abruzzi 24, Turin (TO), Italy

[b] Fluid Mechanics Department, Mondragon University, Loramendi 4, Arrasate, 20500, Spain

[c] Instituto de Investigaciones en Electrónica, Control y Procesamiento de Señales, Universidad Nacional de La Plata, Calle 48 y 116, CC 91, La Plata, Buenos Aires, 1900, Argentina

[d] Ocean and Coastal Engineering Research Group, Department of the Built Environment, Aalborg University, Thomas Manns Vej 23, 1-330, Aalborg, 9220, Denmark

ARTICLE INFO

Keywords:
Wave energy
Wave energy arrays
System identification
Data-based modelling
Control oriented models
Experimental validation

ABSTRACT

One of the key steps towards economic feasibility of wave energy conversion technology concerns scaling up to farms of multiple devices, in the attempt to reduce installation costs by sharing infrastructure, and a consequent drop in levelised cost of energy. Moreover, whenever wave energy systems are deployed in proximity (in so-called *arrays*), the exploitation of the hydrodynamic interactions between single devices is fully enabled, potentially increasing the final energy outcome. To achieve this in real (operational) time, the employed energy-maximising control strategies require control-oriented array models, able to efficiently describe the dynamics of these interconnected systems in a representative fashion. This can be, nonetheless, a difficult task when considering first principles alone, under small motion assumptions, for modelling purposes. Recognising the uncertainty associated to array numerical models obtained from the linearisation of simplified system equations around their equilibria, this paper presents models of several array configurations identified following a frequency domain approach on the basis of experimental data. Tailored tests on laboratory-scale devices have been designed and conducted in the Aalborg University (Denmark) wave tank facility, with the purpose of performing representative system identification of the wave energy systems arrays. The obtained models are validated on different representative sea states configurations, in controlled and uncontrolled motion operational conditions. The validation results are fully discussed and analysed in terms of standard error measures and time lag, while the obtained models are made freely accessible via a linked repository (named *OCEAN*), in the attempt to openly provide validated models for different array configurations.

1. Introduction

Given the increasing world energy demand, the interest for sustainable and renewable energy technologies has grown over the last decades, becoming a crucial topic for research and development (Hosseini, 2020; Nastasi, Markovska, Puksec, Duić, & Foley, 2022). Among the available renewable energy technologies, one with the most (yet still untapped) potential is wave energy (Astariz & Iglesias, 2015; Clément et al., 2002), with around 32000 TWh/year to be potentially exploited (Mork, Barstow, Kabuth, & Pontes, 2010). Part of the obstacles towards technology convergence can be attributed to the large number of different technology solutions currently being explored to solve the wave energy absorption problem (Guo & Ringwood, 2021; Trueworthy & DuPont, 2020). This variety of prototypes and concepts, present in the field, can be certainly attributed to the relatively large number of open issues that must be addressed in the development of economically feasible *wave energy converters* (WECs). Challenges like the variability of the wave energy resource itself (Falcão, 2010; Li, García-Medina, Cheung, & Yang, 2021), the definition of the system employed in the conversion of the physical WEC motion into useful energy (Carapellese, Pasta, Sirigu, & Faedo, 2023; Scavalla, Rossi, La Battaglia, & Pio Belfiore, 2023), or the installation (Vining & Muetze, 2007) and maintenance (Guanche, de Andrés, Losada, & Vidal, 2015; Mérigaud & Ringwood, 2016) of WEC devices, play an important role in the current lack of an efficient and 'strong' technology solution.

* Corresponding author.
E-mail address: edoardo.pasta@polito.it (E. Pasta).

https://doi.org/10.1016/j.conengprac.2024.105949
Received 30 January 2024; Received in revised form 11 April 2024; Accepted 12 April 2024
Available online 17 April 2024

One of the most crucial problems to be solved in the pathway towards economic viability of wave energy technology is the development of effective control strategies (Ringwood, 2020; Ringwood, Zhan, & Faedo, 2023). Wave energy control is responsible for maximising the energy absorbed by WEC devices, while guaranteeing, at the same time, the safety of any mechanism involved in the conversion chain. To fulfil these requirements, the control problem characterising this application is formulated in terms of the optimal computation of the force (or torque) exerted by the actuation system employed in the conversion process to maximise the associated energy conversion output, based on the current wave conditions. Given this *energy-maximising* nature, the wave energy control problem falls under the umbrella of *optimal control* theory. The results of the solution of this optimal control problem directly affect the final *levelised cost of energy* (LCoE), by maximising the annual productivity (Ringwood, Bacelli, & Fusco, 2014), reducing the overall costs of the device (Ströfer, Gaebele, Coe, & Bacelli, 2023), and any immediate need of maintenance actions (Centeno-Telleria, Aizpurua, & Penalba, 2022).

At the state-of-the-art, the vast majority of the control strategies employed to maximise wave energy extraction are *model-based*. In other words, *control-oriented* models, able to describe WEC dynamics, are directly exploited in the control synthesis process. The models employed for this purpose are the result of a trade-off between accuracy and complexity, in the attempt to provide an effective description of the system with low computational burden, guaranteeing real-time feasibility of the numerical solution of the control problem during operations (Faedo, Garcia-Violini, Peña-Sanchez, & Ringwood, 2020; Pasta, Papini, Faedo, Mattiazzo, & Ringwood, 2022). The Navier–Stokes equations (which govern the motion of a body surrounded by a fluid) are usually strongly simplified during the development of these control-oriented models, assuming hypotheses of linearity and/or small oscillations around the system equilibria. As such, the resulting computation associated with any hydrodynamic contributions is usually affected by modelling uncertainty, which can be difficult to quantify (Farajvand, Garcia-Violini, Windt, Grazioso, & Ringwood, 2021). Moreover, the same hypotheses adopted in the modelling stage are inherently invalidated by the application of the optimal control strategies themselves, resulting in the so-called *modelling paradox* (Windt, Faedo, Penalba, Dias, & Ringwood, 2021). In fact, control strategies aimed at maximising the energy extracted by WEC devices tend to emphasise their movement, driving the system outside the range of validity (linearity) used to derive the corresponding models. These issues become even more relevant when, in the attempt to scale up the technology, wave energy converters are deployed in farms (the so-called WEC arrays). In fact, whenever two or more devices are deployed in close proximity, they interact by means of the surrounding wave field. However, this interaction is often modelled assuming the same hypotheses that are considered whenever a single device is modelled, leading to larger uncertainties. Understanding this interaction is of crucial importance for the development of effective control strategies (Garcia-Rosa, Bacelli, & Ringwood, 2015; Li & Belmont, 2014), and for the proper design of the array layouts (Faedo, Peña-Sanchez, Pasta, et al., 2023; Garcia-Rosa et al., 2015). This interaction indeed, which depends (among other factors) on the distance between devices in any given array configuration, can have positive or negative impact on the overall power absorption. As such, not including this interaction in the model employed to synthesise the controller (or modelling it in a not representative manner) affects the energy conversion of the WEC array, leading to suboptimal performances (especially with arrays of close WECs) (O'Sullivan, Sheng, & Lightbody, 2018). The importance of having reliable and representative models of WEC arrays able to describe the dynamics of these systems in operative conditions motivates the application of system identification techniques in an experimental setup. The result of the application of these techniques are models which are more representative of the actual process, and also subject to a lower degree of uncertainty, not being based upon the linearisation of physics equations around an equilibrium. Moreover, in the proposed tests, the identification employs data obtained at different excitation amplitudes, in the attempt to average the system behaviour over the system operational range, instead of assuming the validity of a linearisation around a (rest) equilibrium condition.

1.1. Contributions and paper positioning

Considering the discussion provided in Section 1, this paper presents the application of system identification techniques to model five different array configurations on the basis of data collected during an experimental campaign at the wave tank facilities of Aalborg University, Denmark. The test employed to identify the control-oriented models of the arrays, is designed and performed with the sole purpose of performing data-based modelling of the systems in a wide range of operative conditions. This is done in the attempt of obtaining reliable and representative models, which are not based upon linearisation of physical equations (*i.e.* first principles modelling) or other simplifications. To the best of authors' knowledge, this study represents the first application of system identification techniques to develop models of arrays of wave energy systems purely on the basis of experimental data. The thus obtained models are then validated in uncontrolled and controlled conditions, with the controlled tests performed with both passive and reactive control strategies. To perform the validation tests, three representative sea states are considered (as from the available dataset of tests in Faedo, Peña-Sanchez, Pasta, et al. (2023)), to validate models in different representative irregular wave conditions. Apart from providing a methodology to obtain models of arrays of wave energy systems on the basis of real data, this study makes openly available the resulting validated models. Through the creation of a dedicated repository (termed *OCEAN — Open-access Collection of Experimental wave energy Arrays Nominal models* (Pasta et al., 2024)), it provides reliable models to design controllers for different configurations of arrays of wave energy systems and to study their dynamics. Moreover, these models of real scaled experimental arrays enable fast and extensive simulations, and, for this reason, they can be employed to assess, through a validated tool, the performances of different controllers and array configurations.

1.2. Paper structure

The remainder of this paper is organised as follows. In Section 1.3, the main notation employed through the paper is presented. Section 2 recalls the wave energy optimal control problem, together with the standard modelling assumptions employed for these devices and a brief account of the state-of-the-art of WEC control. In Section 3, the experimental setup adopted during the tests in the wave tank is presented, and the considered array configurations discussed in this study are introduced accordingly. In Section 4, the design of the signals employed in the tests aimed at identifying the representative models of the WEC arrays is discussed, while Section 5 analyses the data-based modelling process and the obtained models for the different array layouts. Section 6 discusses model validation in different conditions (uncontrolled, and controlled by a passive and a reactive controller), describing the validation methodology in detail, and providing validation results in terms of accuracy and lag, based on time-domain data. Finally, Section 7 draws the overall conclusions of this study.

1.3. Notation

The set of non-negative real values is denoted as $\mathbb{R}^+$, while $\mathbb{C}_{<0}$ and $\mathbb{C}^0$ denote the sets of complex values with negative and zero real part, respectively. Unless otherwise stated, if $x \in \mathbb{C}^n$, the notation $x_j \in \mathbb{C}$ denotes the jth entry of x. The eigenvalues of a matrix $A \in \mathbb{C}^{n\times n}$ are denoted as $\lambda(A)$. Given $x \in \mathbb{C}$, the notation $\mathcal{R}\{x\}$ denotes the *real-part* of x, while $\mathcal{I}\{x\}$ is used to define the *imaginary-part* of x. The notation $F(s)$, $s \in \mathbb{C}$, and $F(j\omega)$, $\omega \in \mathbb{R}$, are used for the Laplace

and Fourier transforms of the function f, respectively, provided these are well-defined. The convolution between two functions f and g, with $\{f,g\} \subset L^2(\mathbb{R})$, *i.e.* $\int_{\mathbb{R}} f(\tau)g(t-\tau)\mathrm{d}\tau$, is denoted as $f * g$. Finally, given $\{f,g\} \subset L^2(\Xi)$, $\Xi \subset \mathbb{R}$, their standard inner product is denoted (and defined) as $\langle f,g\rangle_{\Xi} = \int_{\Xi} f(t)g(t)\mathrm{d}t$.

2. Wave energy systems modelling and control problem definition

As discussed within Section 1, wave energy systems are devices aimed at converting the mechanical energy contained in ocean waves into electrical energy, by means of a conversion chain that exploits the device motion generated by the incoming wave field. WECs are usually composed of a floating body (the hull) and a controlled actuation system (the so-called *power take-off*, PTO). The dynamics of these devices are mainly the result of the interaction of the hull with the surrounding fluid and the PTO. Potentially, some inner conversion mechanisms could also be present, characterising, in this way, the conversion chain, and consequently the WEC dynamics (Carapellese, 2023; Scavalla et al., 2023). As already introduced in Section 1, in the attempt to reduce the costs of deployment by sharing infrastructure, multiple devices have to be installed in arrays, trying also to exploit the (eventually constructive) interaction that is generated by their proximity.

Under the hypotheses of frictionless and irrotational flow, linear wave theory, and device displacement significantly smaller than the dimension of the floating body itself, linear potential flow theory can be employed to model the WEC dynamics. With these assumptions, a simplified control-oriented equation describing the motion of an array of N wave energy systems can be formulated as[1]:

$$(m+m_\infty)\ddot{z}_{arr.} + k_r * \dot{z}_{arr.} + s_h z_{arr.} = f_{ex} + u, \tag{1}$$

where $z_{arr.} : \mathbb{R}^+ \to \mathbb{R}^{nN}$, $t \mapsto z_{arr.}(t)$, is the displacement vector of the WEC array (with n degrees of freedom – DoF – considered for each of the N devices), and $m \in \mathbb{R}^{nN\times nN}$ is the generalised inertia matrix (*i.e.* the block diagonal matrix containing the inertia matrix of each device belonging to the array). Following Cummins' formulation (Folley, 2016), the radiation contribution is split into the generalised added mass at infinity frequency $m_\infty \in \mathbb{R}^{nN\times nN}$, and the convolution term $k_r * \dot{z}_{arr.}$, involving the radiation impulse response matrix $k_r : \mathbb{R}^+ \to \mathbb{R}^{nN\times nN}$, $k_{rij} \in L^2(\mathbb{R})$, $\forall\{i,j\} \subset \{1,2,\dots,nN\}$, $t \mapsto k_r(t)$, while $s_h \in \mathbb{R}^{nN\times nN}$ represents the restoring coefficient matrix, employed to model the linear restoring phenomena. Finally, in Eq. (1), $f_{ex} : \mathbb{R}^+ \to \mathbb{R}^{nN}$, $t \mapsto f_{ex}(t)$, is the excitation force[2] vector, while $u : \mathbb{R}^+ \to \mathbb{R}^{nN}$, $t \mapsto u(t)$, represents the control action vector. The terms related to the radiation contribution (m_∞ and k_r) are geometry-dependent and are usually computed numerically by means of boundary element methods (BEMs), see for instance Nemoh (Babarit & Delhommeau, 2015).

Control-oriented models, as the one reported in Eq. (1), are employed in the synthesis of control strategies adopted to define u. As already mentioned in Section 1, WEC controllers are aimed at maximising the energy converted by any given WEC devices, and, for this reason, the control synthesis process is written in terms of an associated *optimal control problem* (OCP). To be precise, this problem is usually formulated as the maximisation of a performance function $\mathcal{J}$, which is a measure of the energy absorbed by the device over a certain time interval $\mathcal{T} = [a,b] \subset \mathbb{R}^+$. A standard formulation of such performance function is given by the absorbed mechanical energy[3]:

$$\mathcal{J}(u) = \frac{1}{T}\int_a^b u(\tau)^\intercal S \dot{z}_{arr.}(\tau)\mathrm{d}\tau, \tag{2}$$

where $T = b-a$, and $S \in \mathbb{R}^{nN\times nN}$ is a diagonal selection matrix, where the terms on the diagonal are used to select the proper device and degree of freedom over which the conversion process effectively takes place. Other performance metrics that are different from the absorbed mechanical energy are also admissible, *e.g.* by taking into account of the net power, or energy at different stages of the conversion chain (for instance, by exploiting *wave-to-wire* (Penalba & Ringwood, 2019; Rosati, Said, & Ringwood, 2023) or *wave-to-grid* (Said, García-Violini, & Ringwood, 2022; Said & Ringwood, 2022) models). Apart from energy-maximisation, WEC controllers are responsible for enabling safe operations and avoid exceeding physical constraints (Bacelli & Ringwood, 2013). In the attempt of ensuring these requirements, *soft constraints* can be implemented via additional terms in $\mathcal{J}$, or *hard constraints* can be formulated along with Eq. (2), as:

$$\begin{cases} |z_{arr.}| \le z_{arr.,max}, \\ |\dot{z}_{arr.}| \le \dot{z}_{arr.,max}, \\ |u| \le u_{max}, \end{cases} \tag{3}$$

for all $t \in \mathcal{T}$, with $\{z_{arr.,max}, \dot{z}_{arr.,max}, u_{max}\} \subset \mathbb{R}^{nN+}$, leading to a constrained optimisation problem. As a consequence, the resulting OCP to be solved in the WEC controller synthesis process can be written as

$$\begin{aligned} u^{\mathrm{opt}} = \arg\max_u \ & \mathcal{J}(u) \\ \text{s.t.:} \\ & \text{WEC dynamics (1)}, \\ & \text{Motion and input constraints (3)}. \end{aligned} \tag{4}$$

Several control strategies have been employed in the WEC control literature (Ringwood et al., 2014) in the attempt of solving the OCP presented in Eq. (4). Among the control applications that are present in the wave energy field, two different classes of strategies can be identified: *optimisation-based* and *non-optimisation-based* controllers (Faedo et al., 2020). The first class (optimisation-based control) includes strategies that require an online numerical solution of the OCP (Eq. (4)) to compute the corresponding control action. This includes (but it is not limited to) *model predictive control* (MPC) (Bracco, Canale, & Cerone, 2020; Jama, Wahyudie, & Noura, 2018; Zhan, Li, Na, & He, 2019), *moment-based control* (Faedo, Peña-Sanchez, Garcia-Violini, et al., 2023; Faedo, Scarciotti, Astolfi, & Ringwood, 2018), and *spectral* and *pseudo-spectral control* (Auger, Merigaud, & Ringwood, 2019; Mérigaud & Ringwood, 2018). Non-optimisation-based control, instead, includes all controllers proposing an approximate realisation of the so-called *impedance-matching* condition (Coe, Bacelli, & Forbush, 2021; Faedo, Carapellese, Pasta, & Mattiazzo, 2022), in the attempt to maximise the overall energy absorption. Examples of controller applications belonging to this class are the *Linear Time Invariant Controller* (LiTe-Con) (Carapellese, Pasta, Paduano, Faedo, & Mattiazzo, 2022; Garcia-Violini, Peña-Sanchez, Faedo, & Ringwood, 2020), and the *Linear Quadratic Gaussian* (LQG) control (Scruggs, Lattanzio, Taflanidis, & Cassidy, 2013; Scruggs & Nie, 2015).

Even if some effort has been put on the development of *model-free* control approaches (Pasta, Faedo, Mattiazzo, & Ringwood, 2023), like *extremum seeking* (Moens de Hase, Pasta, Faedo, & Ringwood, 2021; Parrinello et al., 2020), or *reinforcement learning* (Anderlini, Forehand, Bannon, Xiao, & Abusara, 2018; Anderlini, Forehand, Stansell, Xiao, & Abusara, 2016) most of the control solutions employed in wave energy field are *model-based*, *i.e.* they are based upon a model of the controlled WEC (Pasta, Faedo, et al., 2023). This means that a control-oriented model of the system is required to synthesise the control

[1] From now on, the dependence on t is dropped when clear from the context.

[2] Here the term 'force' is employed in a general sense, to refer to both forces and torques depending on the considered degree of freedom.

[3] Since the focus of this study is related to control-oriented modelling of arrays of multiple devices, note that Eq. (2) is formulated in a generic fashion, enabling, by means of the definition of the non-null terms in the diagonal of matrix S, a *centralised* control formulation (where $\mathcal{J}$ is a measure of the *total* energy absorbed by the array), or a *decentralised* control formulation (where instead, the goal of the control strategy of each device is the maximisation of the energy absorbed by the single device itself, without taking into account of the possible interactions between WECs (Garcia-Rosa et al., 2015)).

strategy itself (as per the definition of the OCP presented in Eq. (4)). In the WEC control loop, models play a role not only in the synthesis of the controller (Pasta, Paduano, Mattiazzo, Faedo, & Ringwood, 2023). In fact, realistic control applications for wave energy systems employ also estimators, in the attempt to estimate the (unmeasurable) force f_{ex} acting on the WEC (Mérigaud & Ringwood, 2018; Peña-Sanchez, Windt, Davidson, & Ringwood, 2020), which are often based upon the same control-oriented models adopted in the control synthesis process. Moreover, whenever predictive control strategies are considered, such disturbances can be forecasted (Nguyen & Tona, 2018; Peña-Sanchez, Merigaud, & Ringwood, 2020), and knowledge of future system behaviour can be also considered when solving the corresponding OCP. In addition, in the same context, models allow the system dynamics to be propagated into the future, enabling constraint handling.

The numerical characterisation of the device based on potential flow theory obtained through BEM solvers assumes motions that can be linearised around an infinitesimally small parameter, usually wave steepness. This condition, and the validity of the models resulting from this assumption, is challenged under controlled conditions, in which the motion tends to be exaggerated by the control action. In fact, performances of model-based controllers can deeply depend on the employed model fidelity in operational conditions. For this reason, if the modelling errors (which could be either parametric or consequence of unmodelled dynamics) are relevant, not only performance is degraded, but the controlled system can behave in an unpredictable manner, causing problems or even jeopardising safe operations. These considerations motivate the adoption of a data-based approach which derives models from real data taken over a range of operative conditions.

3. Experimental wave energy systems array and setup

This section is aimed at describing the experimental setup that has been employed in the performed experiments at Aalborg University facilities. In particular, a precise description of the wave tank facility, together with the instrumentations and the array configurations considered, is provided. This is the same that is presented in Faedo, Peña-Sanchez, Pasta, et al. (2023), where the experimental setup is described, together with the dataset (*SWELL*) of tests employed in this work for validation purposes.

3.1. Wave tank specifications

The presented experimental tests have been performed within the wave tank facilities available at the Ocean and Coastal Engineering Laboratory at Aalborg University, Denmark. The available basin is schematically[4] represented in Fig. 1, together with the positioning of the WECs considered in the tests. The wave tank is composed by a 19.3 m × 14.6 m × 1.5 m (length × width × depth), basin, which has an active testing area of 13 m × 8 m (length × width). A long-stroke segmented *VTI* wavemaker system, composed by 30 individually controlled wave paddles, able to provide also active absorption, is installed in the wave tank. The wavemaker is employed to produce a large variety of sea state conditions with high accuracy (see Vázquez y Torres Ingeniería SL. (VTI) (2024)) in the frequency range of scaled operating conditions of WaveStar devices, which goes from 2 rad/s to 10 rad/s (Faedo, Peña-Sanchez, Pasta, et al., 2023). During the presented tests, the water depth within the tank has been fixed to 0.9 m, while the wavemaker is set to generate long-crested waves, *i.e.* parallel with respect to (w.r.t.) the y-axis, and with a direction of 0° on the x-axis, as indicated within Fig. 1.

Table 1
Main parameters describing a single Wavestar 1:20 prototype considered in the tests.

Parameter	Value
Floater mass	4 kg
Mass moment of inertia w.r.t. A	1 kg m^2
Floater draft	0.110 m
Floater diameter at SWL	0.256 m
Equilibrium position w.r.t. point A θ_A^0	0.523 rad
Distance points A-C L_{AC}	0.412 m
Distance points C-B L_{CB}	0.381 m
Distance points A-B L_{AB}	0.200 m
Distance points A-E L_{AE}	0.484 m
Distance points A-E in y	0.437 m
Distance points A-E in z	0.210 m
Centre of gravity in y	0.415 m
Centre of gravity in z	−0.206 m
Centre of buoyancy in y	0.437 m
Centre of buoyancy in z	−0.321 m
Arm mass	1.157 kg
Arm moment of inertia	0.060 kg m^2

3.2. WEC prototype

The WEC device considered for the presented experimental campaign is a 1:20 scale version of the *Wavestar* wave energy conversion system (Hansen & Kramer, 2011). Four units of this prototype are reported in Fig. 2, together with a schematic of a single Wavestar device. The latter is composed of a floater, which is mechanically hinged to a fixed reference point (**A** in Fig. 2) which is above the *still water level* (SWL). In this way, the WEC is free to move in a single DoF. In equilibrium conditions, the arm connecting the floater to the hinge stands approximately at 30° w.r.t. the SWL. The main physical parameters describing the single prototype can be found in Table 1. The actuation system (*i.e.* the PTO) is an electrical, direct-drive, linear motor (*LinMot Series P01-37 x 240F*), mounted on the upper structural joint composing the device (see Fig. 2). The PTO drive is a *LinMot E1200*, with a force rating up to ±200 N.

3.3. Array configurations

The experimental setup considers the Wavestar prototypes (devices D1 to D4 in Fig. 1) placed within the wave basin by means of supporting structures mounted on a gantry (see Fig. 2). The devices have been installed considering row-like array configurations, with a distance of 39 cm from centre to centre of adjacent devices. This distance corresponds to approximately 1.5 times the diameter of the scaled Wavestar floater (see Table 1), resulting in an inter-device distance (between floaters edges) of approximately one radius, *i.e.* 13 cm. By means of the supporting structure, each device can be lifted out of the water manually, allowing different array configurations depending on the set of devices effectively operating inside the basin.

Five different layout configurations (from L0 to L4), involving up to 3 different devices operating simultaneously within the basin, were considered during the presented experimental campaign (see Fig. 3). This is done in the attempt of investigating the array dynamics and the interaction influence between devices. The choice of the different layouts has been made according to the following lines. The first layout (L0), composed of a single device (D1), has been chosen to provide a baseline case. This is motivated by the previous modelling and validation literature for this specific Wavestar prototype (see, *e.g.* Faedo, Peña-Sanchez, Garcia-Violini, et al. (2023), Garcia-Violini et al. (2021), Hansen and Kramer (2011), Zurkinden, Ferri, Beatty, Kofoed, and Kramer (2014)). This also provides the opportunity of characterise

[4] Note that Fig. 1 is simply a schematic representation of the setup, and objects are not in-scale with respect to the tank dimensions.

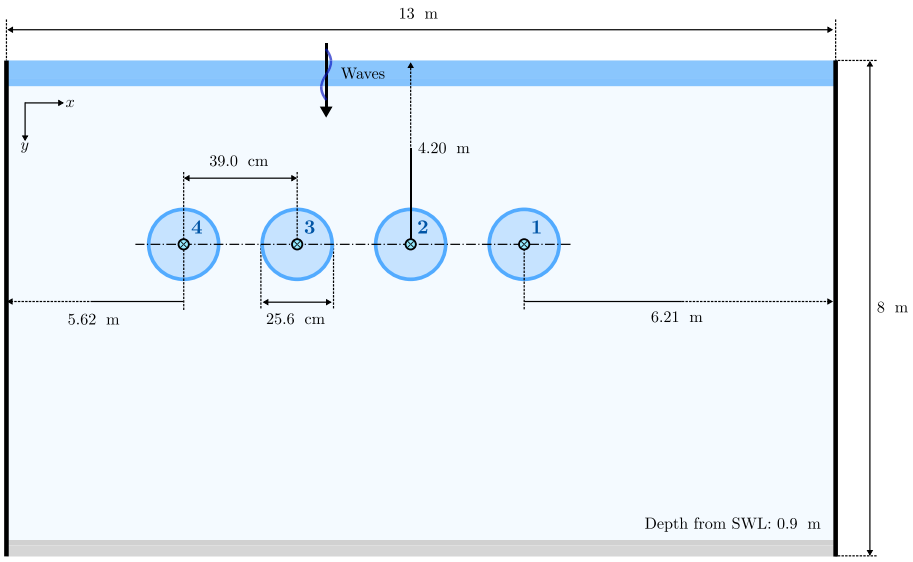

Fig. 1. Schematic representation of the wave basin at the Ocean and Coastal Engineering Laboratory, in Aalborg University. The schematic includes the position associated with each device within the tank. The acronym SWL stands for *still water level*.

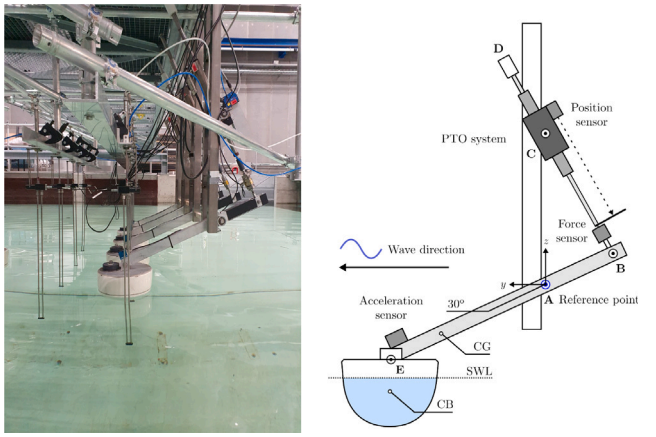

Fig. 2. Picture of the array of scaled Wavestar prototypes, together with a schematic representing the main components of a single device belonging to the considered arrays.

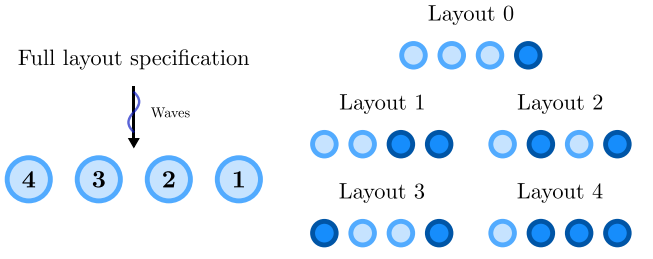

Fig. 3. Schematic of the five different layout configurations considered within the experimental tests. In right side figure, the devices placed inside the water have been represented with a dark blue colour, while the ones lifted outside of the water are presented in light blue. (For interpretation of the references to colour in this figure legend, the reader is referred to the web version of this article.)

experimentally the dynamics of a standard single point absorber device without the influence of other devices in close proximity. The layouts from L1 to L3 instead are aimed at generating and describing array interactions between two devices at different inter-device distances (the distance between the devices centres grows from 39 cm in L1 to 117 cm in L3). The modelling goal of the tests, in this case, is to properly characterise the interaction between the devices and elucidate how this changes with distance. Finally, a layout with three closely arrange devices is considered (L4), extending the L1–L3 layouts, in the attempt to analyse the difference between the interaction among the devices in a more complex layout.

3.4. Acquisition system and available data

The data acquisition system employed during the tests is that described in Faedo, Peña-Sanchez, Pasta, et al. (2023). The target PC employed to handle the overall input/output (I/O) interface is a Speedgoat Real-time Target Machine, connected by means of standard Ethernet to a host PC, transferring data using a user datagram protocol (UDP). Among the input measures, the PTO system translational displacement is both obtained as an output of the PTO driver and measured by means of a dedicated laser position sensor (*MicroEpsilon ILD-1402-600*), for redundancy. The total force that acts on the PTO axis is measured through a load cell (*S-beam Futek LSB302*). Dual-axis accelerometers (*Analog Devices ADXL203EB*) are installed on the deck of the prototype floaters. The information obtained from such accelerometers is exploited, together with the translational motion measurements, to derive rotational motion measurements (*i.e.* angular velocity and displacement) with respect to the fixed reference point **A**, represented in Fig. 2. The measurement data of all variables of interest are acquired at a sample rate of 200 Hz.

The goal of the tests performed as part of this study is to derive control-oriented models describing the dynamical relation that occurs between the total force acting on the PTO axes (*i.e.* the superposition $f_{ex} + u$ in Eq. (1)), and the resulting velocities of the WEC array (*i.e.* $\dot{z}_{arr.}$ in Eq. (1)). In particular, since single-DoF (pitching) devices are considered as part of the array configurations, the input and output variables of interest for each wave energy system are the total torques acting on the device, computed with respect to the x-axis passing through the **A** reference point (see Fig. 2), and the resulting pitching velocities of each device. Considering an array of N devices, the input and output variables are $f_\theta : \mathbb{R}^+ \to \mathbb{R}^N, f_\theta = [f_{\theta,1}, \dots, f_{\theta,N}]^\intercal$ and $v_\theta : \mathbb{R}^+ \to \mathbb{R}^N, v_\theta = [v_{\theta,1}, \dots, v_{\theta,N}]^\intercal$ respectively. As previously discussed within this section, during the experimental campaign, some variables can be directly measured, while others have to be derived from such measurements. In particular, considering the ith device in the array, the measured variables are:

$z_{PTO,i}$: Linear displacement (in m) of the ith device PTO motor. This can be measured either via the incorporated driver sensor, or the laser sensor on top of the PTO axis.

$a_{\mathbf{E},i}$: Linear acceleration (in m/s^2) of the ith WEC floater at its point **E**. This can be measured by virtue of the accelerometer on top of the floater.

$f_{\mathbf{B},i}$: Force (in N) at point **B** of the ith wave energy system in the array. This can be measured directly by the load cell sitting on its PTO axis.

The variables that instead can be reconstructed or estimated for the ith device in the array are:

$f_{\theta,i}$: Total torque (in Nm) reconstructed with respect to point **A** of the ith device (*i.e.* the sum $f_{ex,i} + u_i$).

$z_{\theta,i}$: Angular displacement (in rad) of the ith device reconstructed with respect to point **A** of the ith device.

$v_{\theta,i}$: Angular velocity (in rad/s) of the ith device reconstructed with respect to point **A** of the ith device.

$a_{\theta,i}$: Angular acceleration (in rad/s^2) of the ith device reconstructed with respect to point **A** of the ith device.

Among these variables, $f_{\theta,i}$, $z_{\theta,i}$, and $a_{\theta,i}$ can be reconstructed by means of geometrical relations with the measured variables presented above (as done in *e.g.* Ringwood et al. (2019)), *i.e.*:

$$f_{\theta,i} = f_{\mathbf{B},i} \cos\left(\sin^{-1}\left(\frac{L_{\mathbf{AC}}^2 - L_{\mathbf{AB}}^2 - (L_{\mathbf{BC}} + z_{PTO,i})^2}{-2L_{\mathbf{AB}}^2(L_{\mathbf{BC}} + z_{PTO,i})}\right)\right) L_{\mathbf{AB}}, \tag{5}$$

$$z_{\theta,i} = \theta_{\mathbf{A},\mathbf{i}}^0 - \sin^{-1}\left(\frac{(L_{\mathbf{BC}} + z_{PTO,i})^2 - L_{\mathbf{AC}}^2 - L_{\mathbf{AB}}^2}{-2L_{\mathbf{AC}}L_{\mathbf{AB}}}\right), \tag{6}$$

$$a_{\theta,i} = \frac{a_{\mathbf{E},i}}{L_{\mathbf{AE}}}. \tag{7}$$

The last remaining variable, $v_{\theta,i}$ requires an estimation process. With this goal, the available measures are employed, together with a Kalman Filtering (KF) technique (see Chui and Chen (2017)) to estimate the array angular velocities v_θ. Note that the same approach for the estimation of v_θ has been employed accordingly in *e.g.* Tona, Sabiron, Nguyen, Mérigaud, and Ngo (2020), Zurkinden et al. (2014), for the same prototype device.

4. Tests design

To obtain the control-oriented models of the different wave energy system arrays, a *black-box* system identification process (Schoukens & Ljung, 2019) is performed in this study. In particular, a *frequency-based* approach is considered, following different steps:

1. Several different identification signals are applied to the available system inputs, and the outputs are recorded. More in particular, in each test, the identification signals are applied one by one to each device of the array, recording the measured output for each device. In this way, the relation from every input to every output of the array is measured. An illustrative example of the inputs and outputs tests for the L4 array is presented in Fig. 4, showing the three input signals (and resulting outputs in the array) applied to each L4 device.
2. Considering the frequency response functions resulting from the input and output measurements, the average of these is computed, obtaining the so-called average *empirical transfer function estimate* (ETFE).
3. A parametric dynamical model of the array is computed, by fitting its frequency response to the ETFE obtained at step 2.

As highlighted in the first step of this process, each system input channel is excited several times by means of different signals. These signals differ in amplitude, in the attempt to obtain, through an averaging process, a *representative linear model* of the system in operative (controlled) conditions. Wave energy systems indeed, as discussed in Section 1, tend to present an amplified motion whenever they are controlled by means of an energy-maximising strategy (Windt et al., 2021). For this reason, the obtained model needs to take into account different levels of excitation amplitude in the identification process, to provide a representative dynamical structure for control purposes.

Being the excitation signal f_{ex} in Eq. (1) characterised by a spectrum whose broadness depends on the deployment site (Hasselmann et al., 1973; Pierson & Moskowitz, 1964), the WEC system is constantly excited over a certain range of frequencies. For this reason, during the system identification process, it is important to properly excite the system, in the attempt to characterise the system behaviour in operational conditions. To do this, a sufficiently Mareels (1984) and persistently Willems, Rapisarda, Markovsky, and De Moor (2005) exciting signal must be employed in the identification tests. For this reason, *down-chirp* signals are employed (Ljung, 1999), in the attempt of covering the frequency range of interest during the experimental test. The choice of a linearly decreasing frequency in the generation of the chirp signal is motivated by the need of minimising the effects of reflected waves in the wave basin during the tests (see the arguments in Faedo et al. (2024)).

Due to their multi-device nature, WEC arrays can be seen as *multiple-input and multiple-output* (MIMO) systems. For this reason, considering the total torques f_θ as the inputs of the system, and the array velocities v_θ as the corresponding outputs, to perform the identification, the tests are performed applying the chirp torque signal one by one to the devices belonging to the array, and measuring the resulting velocities in all the devices involved in any given configuration. It is important to notice that these tests are performed in still water, *i.e.* without the presence of waves within the basin, and each torque signal is applied via the PTO system only to the single device being externally excited, while the rest of the array devices are only excited by the hydrodynamic coupling with the excited device, as shown in Fig. 4.

To be precise, let the test torque inputs set applied to the jth device be defined as $\mathscr{F}_{ID,j} = \{f_{ID,j}^1, \dots, f_{ID,j}^P\} \subset \mathbb{R}$, with $P \in \mathbb{N}^+$ the number of amplitudes considered in the identification. Each $f_{ID,j}^p$ signal in $\mathscr{F}$ corresponds with an identification chirp torque of amplitude $A^p \in \mathscr{A}_{ID} = \{A^1, \dots, A^P\} \subset \mathbb{R}^+$ applied to the jth device of the array, and the resulting angular velocity measured at the ith device is denoted as $v_{\theta,i,j}^p$. In test conditions, where the water is still and no excitation force is applied (*i.e.* $f_{ex} = 0$ since no wave is facing the devices), the total external torques correspond only to that applied by the PTO, *i.e.*, considering the test with pth amplitude on the jth device, with $f_{\theta,j} = f_{ID,j}^p$. An example of the identification tests is presented in Fig. 4, where chirp signals of amplitude 4 Nm are applied, one by one, to the three devices composing L4 (each column corresponds to a single test, and each row is a device).

As it is possible to notice, whenever an identification signal is applied to a device, the others are not excited by any external torque. However, these are still moving due to the corresponding interaction between array devices due to radiation. Each of the chirp signals lasts 140 s, and spans the frequency range that goes from 0.01 rad/s to 75 rad/s. The choice of these frequencies is made in the attempt to excite the system in a range of frequencies that safely include all possible operational conditions, without any risk of 'transient effects' that could possibly compromise the identification process during the frequency swipe. The set of amplitudes that have been tested in the identification experiments is $\mathscr{A}_{ID} = \{1.5, 2.0, 2.5, 3.0, 3.5, 4.0\}$ Nm. These amplitudes are designed to effectively excite the system in the amplitude range that characterise the operation of these wave energy systems (in both controlled and uncontrolled conditions). The resulting identification signal spectra, and a zoomed view of the corresponding time signals, are shown in Figs. 5 and 6.

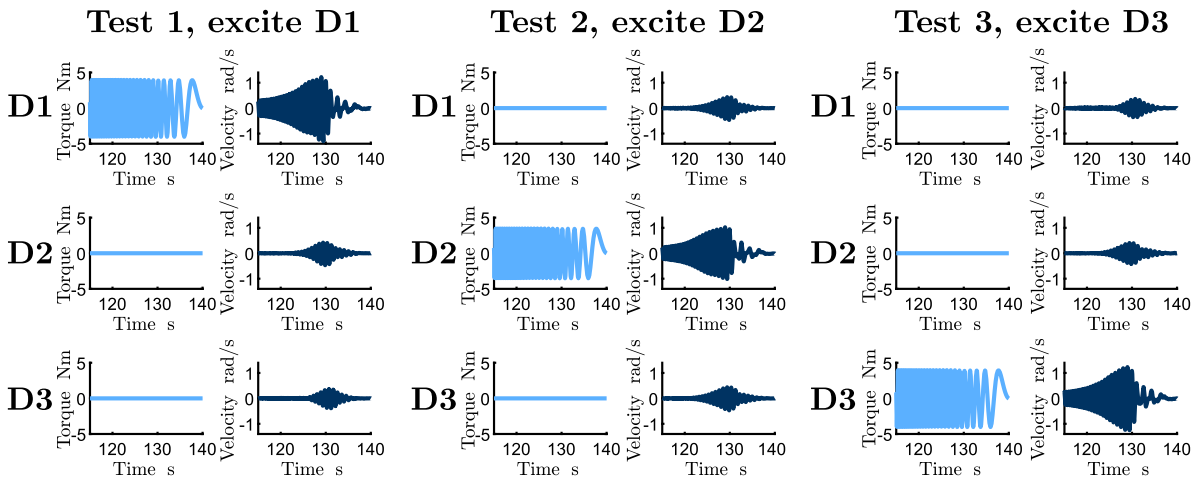

Fig. 4. Example of system identification experimental tests: the chirp-signal of an amplitude of 4 Nm is applied to each of the three devices of the L4 array, one by one. In the figure, each column corresponds to a single test, and each row is a device.

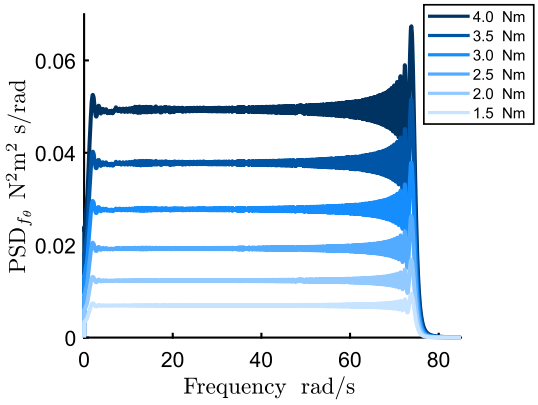

Fig. 5. Spectra of the chirp signals employed in the identification tests.

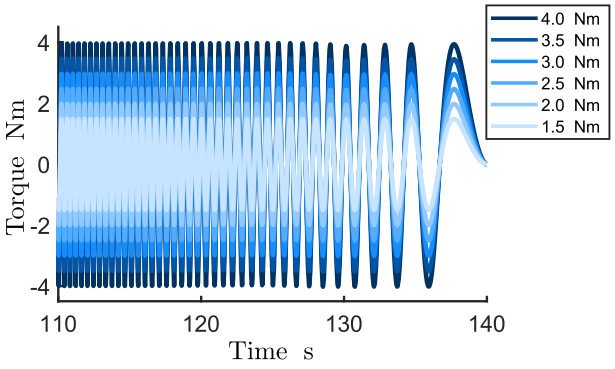

Fig. 6. Zoomed view of the last 30 s of the chirp signals employed in the identification tests.

5. Experimental modelling of wave energy systems arrays

As described in Section 4, for each array layout, different identification signals are applied to each device separately, in the attempt to obtain the system frequency responses at different levels of excitation. Following these experiments, for each I/O combination of the array, the obtained frequency responses are averaged to compute the corresponding ETFE that is employed in the identification process. For each excited device, in each array layout, five different excitation amplitudes have been tested and considered in the averaging process that computes the ETFE employed in the identification.

This study proposes to compute, as a result of the process of identification, a *state-space* model of each array layout, compatible with modern control strategies. Defining a general identified state-space model as:

$$G_{id.,arr.} : \begin{cases} \dot{x} = & Ax + Bu, \\ y = & Cx, \end{cases} \tag{8}$$

with $A \in \mathbb{R}^{n_{st.} \times n_{st.}}$, $B \in \mathbb{R}^{n_{st.} \times n_{in.}}$, and $C \in \mathbb{R}^{n_{out.} \times n_{st.}}$ (with $n_{st.}$, $n_{in.}$, and $n_{out.}$ the order of the identified system, number of inputs, and number of outputs, respectively), the identification is performed by solving a minimisation process essentially formulated as

$$\begin{aligned} &\min_{(A,B,C)} \left\| C(j\omega - A)^{-1} B - G_{ETFE}(j\omega) \right\|_2^2, \\ &\text{s.t.:} \\ &\omega \in \Omega_{ID}, \\ &\mathcal{R}\{\lambda(A)\} \subset \mathbb{R}^- \end{aligned} \tag{9}$$

with $G_{ETFE}(j\omega)$ the ETFE of the array layout that is being modelled, and Ω_{ID} the set of frequencies over which the subspace-based identification is performed (McKelvey, Akcay, & Ljung, 1996). The second constraint in (9), which is related to the eigenvalues of the A matrix, is to force the identified system to be stable. For each layout, a different set of frequencies is considered in the formulation of the problem in Eq. (9), as different model orders and set of amplitudes $\mathcal{A}$ are considered in the computation of the ETFE. This information can be found, for each layout, in Table 2.

As it is possible to see from Table 2, the model order has been defined (following an approach that aims at the best compromise between accuracy and complexity) as 8 for all the array configurations, while L0 (*i.e.* the single device) the best compromise is found with a 6th-order model. The possibility of describing an array system with a reduced order suggests the fact that different devices in the array effectively share part of their internal modes. Regarding the frequency range employed in the identification, as it can be seen from Table 2, in the case of the single device (L0), or with two physically close devices (L1), the best value (in terms of validation error) for the minimum frequency $\omega_{min.}$ of the frequency range over which the frequency response of the identified system is computed (see Eq. (9)) is obtained at a lower frequency than the reminder of the configurations (0.05 rad/s as opposed to 0.1 rad/s), while in the configuration with three devices (L4) the best maximum value $\omega_{max.}$ is higher (20 rad/s as opposed to 15 rad/s).

Table 2
Identified model design parameters: for each array layout, the devices employed (Dev. ID), the model order (Mod. order), the minimum and maximum values of the frequency range employed in the identification ($\omega_{min.}$ and $\omega_{max.}$ respectively), are presented together with the amplitude of the identification signals adopted in the computation of the ETFE. The amplitudes employed with D1, D2, and D3 are labelled with the following dots: ●, ●, ●.

Dev. ID			Layout	Mod. order	Ω_{ID}, rad/s		$\mathcal{A}$ used tests, Nm					
D1	D2	D3			$\omega_{min.}$	$\omega_{max.}$	1.5	2.0	2.5	3.0	3.5	4.0
1			L0	6	0.05	15	●	●	●	●	●	
1	2		L1	8	0.05	15		●●	●●	●●	●●	●●
1	3		L2	8	0.1	15		●●	●●	●●	●●	●●
1	4		L3	8	0.1	15		●●	●●	●●	●●	●●
1	2	3	L4	8	0.1	20	●	●●	●●	●●	●●	●●

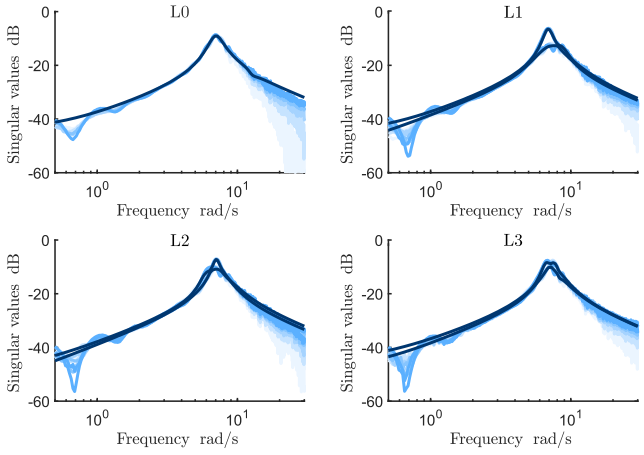

Fig. 7. Sigma plot of L0, L1, L2, L3. Dark blue lines describe the singular values of the identified systems, while light blue lines are the frequency responses of the identification tests at different amplitudes. (For interpretation of the references to colour in this figure legend, the reader is referred to the web version of this article.)

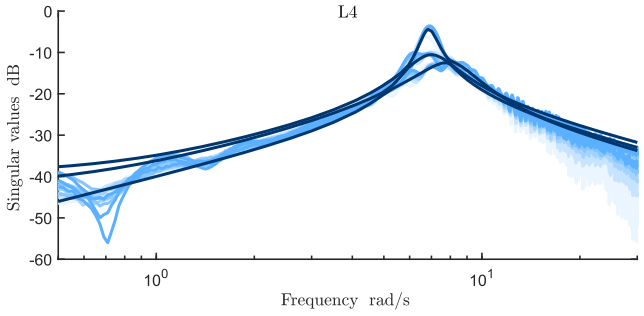

Fig. 8. Sigma plot of L4. Dark blue lines describe the singular values of the identified systems, while light blue lines are the frequency responses of the identification tests at different amplitudes. (For interpretation of the references to colour in this figure legend, the reader is referred to the web version of this article.)

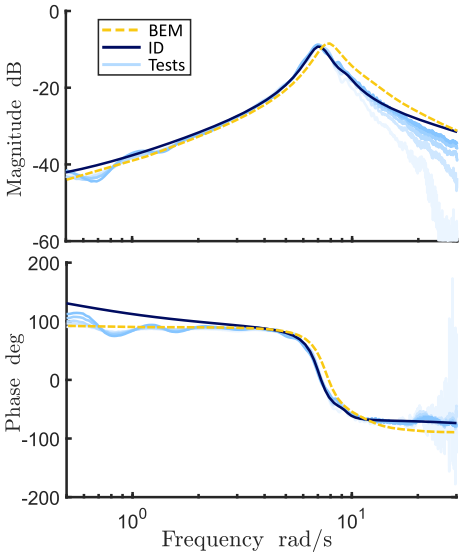

Fig. 9. Bode diagram for the L0 array layout. Dark blue lines describe the Bode diagram of the identified system, while light blue lines are the frequency responses of the identification tests at different amplitudes. The yellow lines represent the Bode diagram of the model based on linearisation obtained from BEM solvers. (For interpretation of the references to colour in this figure legend, the reader is referred to the web version of this article.)

Finally, the set of amplitudes for the signals employed in the computation of the ETFE is, apart from the case of D1 in L0, and D2 in L4, composed by five signals with amplitudes $\mathcal{A} = \{2.0, 2.5, 3.0, 3.5, 4.0\}$ Nm. The resulting velocities from these amplitudes better describe the range of operation of the system under operative conditions. In the L0 case, being a single device, the energy injected into the system by means of the identification signal is not dissipated through a coupled device (as done in L1, L2, L3, L4), and, for this reason, the highest amplitude value (*i.e.* 4.0 Nm) puts the system outside realistic operating conditions (and, in this way, to $\mathcal{A} = \{1.5, 2.0, 2.5, 3.0, 3.5\}$ Nm). On the contrary, due to the strong coupling phenomena that characterise D2 in L4 (it is the central device in an array of three closely placed devices), constructive phenomena are present at resonance frequency, leading to motions outside operating conditions for the velocity of this device whenever the signal with highest amplitude value is applied (hence, for this device, $\mathcal{A} = \{1.5, 2.0, 2.5, 3.0, 3.5\}$ Nm). The *sigma* plots describing the singular values of the frequency responses associated to each different tests and identified models of the array layouts are shown in Figs. 7 and 8. In these figures, dark blue lines describe the singular values of the identified systems, while light blue is used to denote the frequency responses of the identification tests at different amplitudes. As it can be seen from these figures (Figs. 7 and 8), the resonance frequency of the system whenever the configuration is made of 1, 2 or 3 devices remains virtually identical to that characterising the single (standalone) device, *i.e.* $\omega \approx 7.1$ rad/s.

To further extend the results presented in Figs. 7 and 8, the Bode plot of the identified systems for L0, L1, and L4 are shown in Figs. 9, 10, and 11, respectively. As it can be seen from these figures, the identified models are able to properly fit the frequency response in the range of frequencies that characterise the operating conditions. In these conditions, indeed, the system is excited in the range of frequencies that goes from $\omega \approx 2$ rad/s to $\omega \approx 10$ rad/s. As it is also possible to notice, wave energy systems are designed to have their resonance condition included in their operating range. Since these models are identified to be directly employed in the synthesis of an associated control strategy, and because the latter attempts to replicate the so-called impedance-matching condition, which is characterised (in the unconstrained condition) by a null phase behaviour between the wave

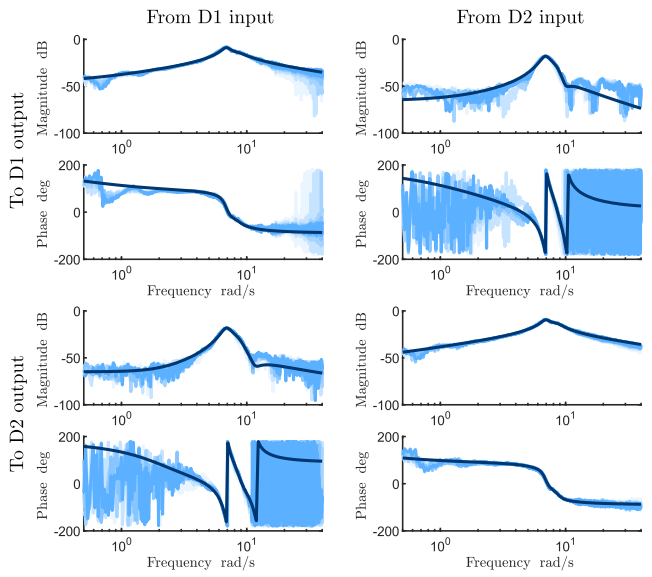

Fig. 10. Bode diagram for the L1 array layout. Dark blue lines describe the Bode diagram of the identified system, while light blue lines are the frequency responses of the identification tests at different amplitudes. (For interpretation of the references to colour in this figure legend, the reader is referred to the web version of this article.)

excitation force f_{ex} and the resulting velocity of the controlled wave energy system v_θ (Faedo et al., 2022; Ringwood et al., 2014), the fitting of the phase (and a consequent small delay/lag in the validation) of the frequency responses is of particular interest. As shown by Figs. 9, 10, and 11, the phase effectively matches well that one obtained by the empirical experimental frequency responses in the frequency range of interest. Moreover, in Figs. 10 and 11, *i.e.* in the cases with multiple devices, it is possible to appreciate that, even if small, differences in the frequency responses of the devices (and of their coupling) are present. This phenomenon, caused by the (slight) differences between devices and by their position in the array (for the L4 case), justifies the proposed approach, in which the input signal is injected, one by one, in all the array devices. Fig. 9 also shows the difference between the identified model and the model obtained through linearisation and numerical characterisation based on potential flow theory (by means of BEM solvers). As can be noticed, the BEM-based model is not able to match the frequency responses observed experimentally, especially in a neighbourhood of the resonance behaviour. Moreover, the resonance peak characterising the experimental data, and that associated with the BEM-based model, do not correspond, with a difference of approximately 1 rad/s. The uncertainty introduced by these mismatches between BEM-based model and the real device (especially in terms of the phase representation) could potentially jeopardise safe operations. Additional considerations can be made regarding the coupling between devices. First of all, the magnitudes of the coupling I/O relations are not negligible if compared to the ones diagonal elements of the overall I/O response matrix, especially in the resonance area. This motivates the importance of including such coupling effects within any control-oriented models. Moreover, as shown in Figs. 10 and 11, in the range of frequency in which the motion of the system is not largely amplified (*i.e.* in the frequencies that are not close to resonance), the quality of the frequency response of the coupling relations rapidly degrades since, at these frequencies, the excited devices do not influence the reminder of the array via the radiation effects, *i.e.* coupling effects are negligible. Finally, as the distance form the excited device increases, the water itself dissipates the generated radiation effects, as it can be noticed in Fig. 11. In this figure, indeed, whenever D1 or D3 are excited, the coupling I/O relations have a lower magnitude at higher distances (*i.e.* D3 moves less than D2 when D1 is excited, and D1 movement is smaller than that corresponding to D2 when D3 is excited).

Table 3
Characteristics of the irregular wave condition employed in the validation. For each sea state (Wave ID), the characteristics of its JONSWAP spectrum (peak period T_p, significant height H_s, and peak enhancement factor γ), are reported, together with the signal length.

Wave ID	T_p, s	H_s, m	γ	Length, s
SS1	1.4122	0.063	3.3	300
SS2	1.836	0.104	3.3	300
SS3	0.988	0.0208	1	300

Table 4
Control parameters: proportional (θ_1) and integral (θ_2) coefficients adopted in the control law in Eq. (10) in the different wave conditions (Wave ID), and for the different control strategies (P and PI).

Wave ID	P		PI	
	θ_1, Nms/rad	θ_2, Nm/rad	θ_1, Nms/rad	θ_2, Nm/rad
SS1	9.57	0	2.74	−32.31
SS2	16.74	0	4.14	−24.73
SS3	2.81	0	2.79	−2.59

6. Models validation

In this Section, the models obtained through the process described in Section 5 are validated in both uncontrolled and controlled conditions, to assess their overall performance and accuracy. To do this, the wave excitation forces, control parameters, and motion data, are directly extracted from the SWELL open-access dataset (Faedo, Peña-Sanchez, Pasta, et al., 2023), obtained during the same experimental campaign presented in this study. During this experimental campaign, three different irregular waves have been tested, with experimental normalised spectra shown in Fig. 12. Three irregular sea state conditions (each lasting 300 s) have been tested, named SS1, SS2, and SS3, generated in terms of the JONSWAP spectra (Hasselmann et al., 1973) (peak period T_p, significant height H_s, and peak enhancement factor γ) presented in Table 3.

The validation of the system under controlled conditions is performed here by validating the *closed-loop system*, *i.e.* by coupling the identified models with the same (feedback) control strategies and parameters employed in the tests within SWELL, and by applying, to this controlled system, the measured external wave excitation force f_{ex} (see Faedo, Peña-Sanchez, Pasta, et al. (2023)). The resulting motion is then compared to the experimentally measured controlled motion of the device in the same operating input wave. The system in controlled conditions has been tested with two controllers: a *proportional* (P) and a *proportional–integral* (PI) structure. The former has been employed to validate the model when it is controlled by a *passive* strategy, while the latter is used to validate the model when controlled by a *reactive* control action (Ringwood et al., 2023). The two control laws employed to compute the control action of the ith device in the array are, in this way, defined by the following structure

$$u_i(v_{\theta,i}, z_{\theta,i}, \theta) = \theta^\top \begin{bmatrix} v_{\theta,i} \\ z_{\theta,i} \end{bmatrix}, \tag{10}$$

where $\theta^\top = [\theta_1, \theta_2]$ is the vector containing the proportional and integral coefficients (θ_1 and θ_2 respectively). As a consequence, in the P-control case, the integral term (defined by θ_2) is set to 0. The coefficients employed in the control of the arrays in the different sea state conditions are recalled in Table 4.

To assess the quality of the obtained models in the different conditions, two policies are employed. In particular, to quantify the error between the output of the models and the measured velocities, the *Normalised Mean Absolute Percentage Error* (NMAPE) is employed. This is computed as:

$$\text{NMAPE}_i = \frac{100}{N_{samp.}} \sum_{k=1}^{N_{samp.}} \frac{|v_{\theta,i}(kT_s) - \hat{v}_{\theta,i}(kT_s)|}{\max\left(|v_{\theta,i}|\right)}\%, \tag{11}$$

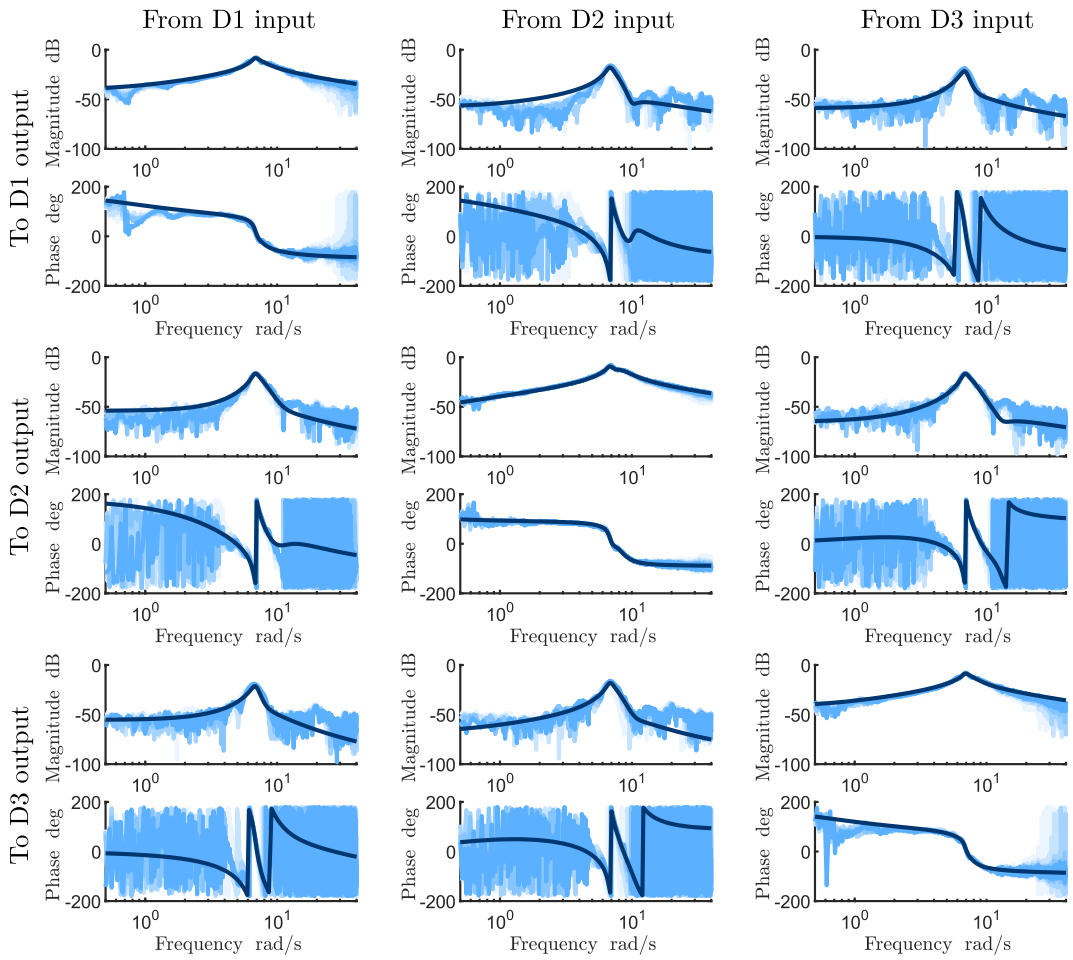

Fig. 11. Bode diagram for L4 array layout. Dark blue lines describe the Bode diagram of the identified system, while light blue lines are the frequency responses of the identification tests at different amplitudes. (For interpretation of the references to colour in this figure legend, the reader is referred to the web version of this article.)

Table 5
NMAPE (%) of the identified models in validation conditions (Wave ID: SS1, SS2, SS3). For each device (Dev. ID) in the identified array configurations (L0, L1, L2, L3, and L4), the NMAPE is reported in uncontrolled motion (UM), and controlled one under proportional (P) and proportional–integral (PI) control conditions.

Wave ID	Dev. ID	L0			L1			L2			L3			L4		
		UM	P	PI	UM	P	PI	UM	P	PI	UM	P	PI	UM	P	PI
	D1	6.01	2.57	3.44	3.93	2.61	3.08	7.99	3.45	3.65	5.39	3.64	3.54	5.1	2.96	3.97
SS1	D2				3.36	2.16	3.18	5.42	3.17	2.9	4.65	2.2	2.93	5.2	2.04	2.94
	D3													3.85	2.66	2.55
	D1	5.99	2.45	3.84	5.52	3.75	4.15	6.42	4.38	4.92	2.33	3.62	5.17	5.48	3.6	4.85
SS2	D2				5.32	3.75	4.11	5.47	3.84	4.77	1.62	3.54	5.77	5.54	2.64	3.24
	D3													4.99	3.13	3.5
	D1	6.87	7.91	9.62	6.4	8.62	7.35	6.53	6.46	6.94	6.43	8.5	7.91	7.2	10.35	7.29
SS3	D2				3.82	5.63	3.73	6.48	6.15	6.92	8.28	9.02	8.49	6.49	8.31	4.48
	D3													7.21	9.85	7.07

Table 6
Delay (in ms) of the identified models in validation conditions (Wave ID: SS1, SS2, SS3). For each device (Dev. ID) in the identified array configurations (L0, L1, L2, L3, and L4), the delay is reported in uncontrolled motion (UM), and controlled one under proportional (P) and proportional–integral (PI) control conditions.

Wave ID	Dev. ID	L0			L1			L2			L3			L4		
		UM	P	PI	UM	P	PI	UM	P	PI	UM	P	PI	UM	P	PI
	D1	40	10	15	15	−5	20	55	25	20	25	25	15	30	20	25
SS1	D2				10	−5	25	35	15	15	20	5	10	20	15	15
	D3													15	10	10
	D1	20	−5	−5	25	30	25	25	45	35	50	25	30	10	25	20
SS2	D2				15	30	35	5	35	35	25	25	40	0	15	15
	D3													−5	15	10
	D1	−25	−30	−50	−10	−35	−25	10	−10	−15	5	−45	−35	−20	−60	−25
SS3	D2				−5	−25	−10	−15	−15	−30	−35	−55	−50	−10	−45	0
	D3													−15	−50	−10

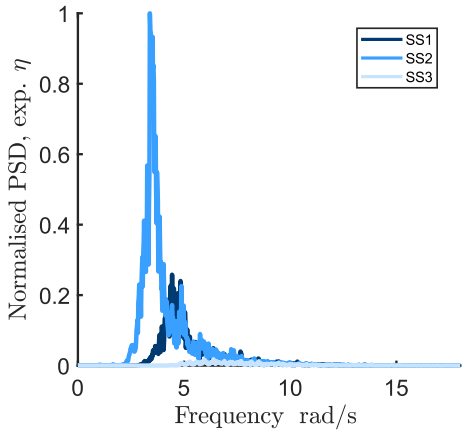

Fig. 12. Normalised power spectral density of the wave elevation η experimentally measured during the test. Three irregular sea state conditions have been tested, named SS1, SS2, and SS3.

where, given the sea state condition employed in the validation, NMAPE_i is the NMAPE computed for the ith device of the array, $N_{samp.}$ is the length (in terms of number of samples) of the validation signal, T_s is the sampling period, and $\hat{v}_{\theta,i}$ is the output of the same ith device, computed by the identified model. Another important aspect that must be considered in the validation of control-oriented models of wave energy systems, is the delay between the measured signal and the output of the identified models (Faedo, Peña-Sanchez, & Ringwood, 2021). This quantity has been assessed through cross-correlation between the two signals ($v_{\theta,i}$ and $\hat{v}_{\theta,i}$), as in Peña-Sanchez, Windt, et al. (2020). The results of the validation, for each layout and conditions considered (uncontrolled motion – UM – and under proportional – P – and proportional–integral – PI – control) are reported in Tables 5 (NMAPE) and Table 6 (delay).

Regarding the validation error, it is possible to highlight how the approach adopted in this study, in which the different frequency responses that span the operational range of velocities and forces of the device are averaged, is effectively reducing the error measured in controlled conditions whenever a reactive controller (PI in this case) is applied. The highest errors indeed, are measured in the uncontrolled motion (UM) conditions. It is important to remind that, whenever an energy-maximising control is deployed (as in this case), the motion of the system is amplified, and for this reason, the models that are based on linearisation of equations around the equilibrium position usually perform worse. Having in mind that the presented models are aimed at synthesising energy-maximising control strategies (and not directly at describing the system in uncontrolled motion), an approach that aims at describing in a better way the dynamics of the array systems in wider ranges of operation (as the one proposed here), is, in this way, justified. For similar reasons, among the different wave conditions, the highest errors are present in the third sea state (SS3). Due to its low value of H_s and γ (see Table 3 and Fig. 12) the wave itself provides less excitation to the system, and its energy is also spread over a wider range of frequency. As a consequence, the motion range is reduced with respect to that generated by the reminder of the sea state conditions (SS1 and SS2). Since the frequency responses employed in the modelling stage are produced by larger motions than those induced by this wave conditions, the errors in validation are effectively higher than for the rest of the sea states considered. In general, the average NMAPE is about 5% (5.4%, 4.4%, 5.3%, 5.1%, 5.0% for L0, L1, L2, L3, and L4 respectively), which is a value that is acceptable for a linear control-oriented models of wave energy arrays (see *e.g.* Faedo et al. (2024)).

Regarding any presence of delay, similar considerations on the obtained values in validation can be made. For this kind of devices a practical control sampling rate is about 25 Hz (see Faedo et al. (2024), Faedo, Peña-Sanchez, Garcia-Violini, et al. (2023) for experimental assessments on these prototypes), which corresponds to a sampling

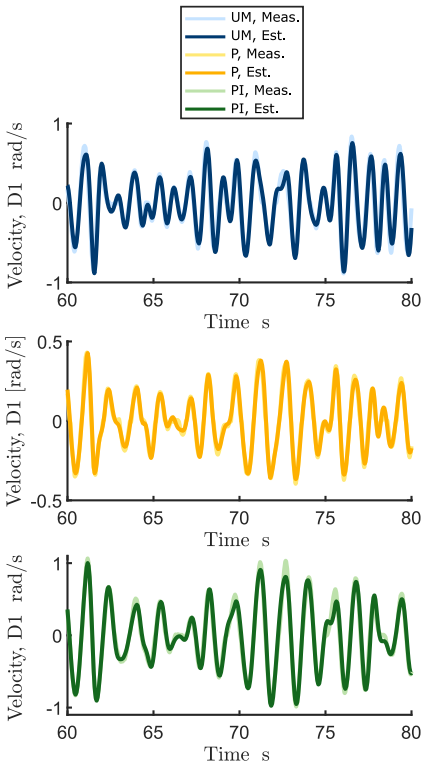

Fig. 13. Comparison of the measured (Meas.) and estimated (Est.) velocities with a single device (L0 configuration) during the validation process, in uncontrolled motion (UM), and controlled one with a proportional (P) and proportional–integral (PI) strategy. The zoomed figures show 20 s of validation with the SS1 wave condition.

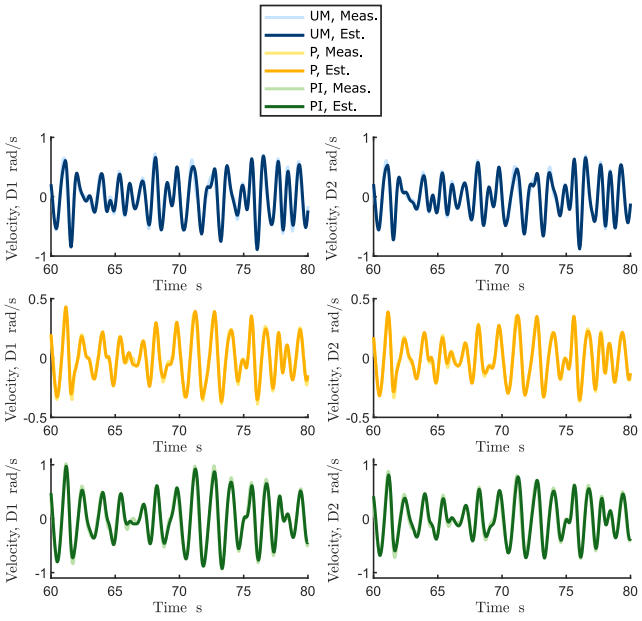

Fig. 14. Comparison of the measured (Meas.) and estimated (Est.) velocities of L1 array configuration during the validation process, in uncontrolled motion (UM), and controlled one with proportional (P) and proportional–integral (PI) strategies. The zoomed figures show 20 s of validation with the SS1 wave condition.

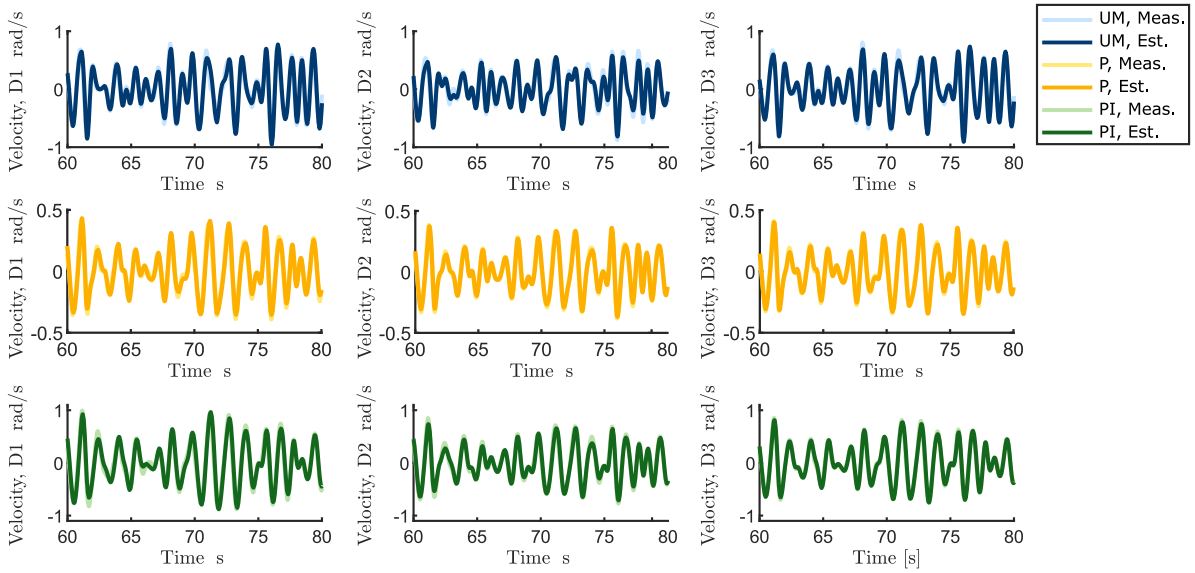

Fig. 15. Comparison of the measured (Meas.) and estimated (Est.) velocities of L4 array configuration during the validation process, in uncontrolled motion (UM), and controlled one with proportional (P) and proportional–integral (PI) strategies. The zoomed figures show 20 s of validation with the SS1 wave condition.

period of 40 ms. Having said that, the results shown in Table 6 are effectively compatible with the dynamics described by the optimal control strategy. The average absolute value of the delay measured during the validation is about 22 ms (22.2 ms, 19.4 ms, 24.4 ms, 28.8 ms, 18.8 ms for L0, L1, L2, L3, and L4 respectively), which is significantly smaller than the sampling period of the controller. The highest delay values are observed, similarly to the NMAPE, whenever the devices are operating in SS3 wave conditions. However, even in these conditions, the worst mismatch between the measured velocity and the estimated one is at most 60 ms, which is still less than 2 time steps for the controller, not really implying strong consequences in the optimality of the control strategy.

In Figs. 13, 14, and 15, the validation signals are compared in all three conditions (uncontrolled motion, and controlled one with a P and PI strategies) for L0, L1, and L4 configurations. As it can be appreciated from these figures, the PI condition, as mentioned before, is the one, in general, generating the largest motions for the devices involved. On the contrary, the simple passive controller, being effectively an additional damping for each device, results in a reduced motion of the overall array. Regarding the phase mismatch (which plays a big role in the energy maximisation process for wave energy systems), the models show a limited delay, which is mostly observed in small motion regions. In general, the models are able to properly describe the dynamics of the arrays, even with limited model orders (and consequent reduced complexity, which is fundamental for real-time control purposes). This result makes this approach suitable for modelling arrays of wave energy systems in which nonlinearities are effectively changing the overall dynamics, but they are still non-dominant when compared to the linear behaviour of the system. In those cases in which, instead, the nonlinear behaviour prevails, other approaches, like nonlinear system identification should be pursued (Schoukens & Ljung, 2019). Finally, it is important to highlight that validating the model in controlled conditions allows the assessment not only of the overall model performance, but also its compatibility with the ultimate objective of synthesising feedback controllers for WEC arrays systems.

7. Conclusions

This study provides the experimental results of the application of a data-based approach for modelling wave energy systems array in a wave basin, via system identification procedures. In particular, the results coming from system-identification-oriented tests are employed to model five different array layouts (with up to three devices in close proximity), and the obtained models have been validated in both controlled and uncontrolled conditions, over a set of three different irregular wave inputs. The system, in controlled conditions, is controlled by means of passive (proportional P control) and reactive (proportional–integral PI control) strategies, to assess the model performance in realistic operative conditions. A frequency-based system identification approach is applied over a set of tests with different amplitudes, in the attempt to obtain models able to describe the range of operation amplitudes accurately, as opposed to standard modelling based on the linearisation of physics-based equations. The results show, in average, an error of $\sim 5\%$ and a delay of $\sim$20 ms (which is effectively smaller than the control sampling time employed in real-time control implementations on the same devices). Furthermore, recognising the role of control-oriented models in the development of efficient wave energy systems, and the need of validated models of arrays of devices, this study provides (in an open-source fashion) the obtained models, in the attempt to reduce the uncertainty associated to the control laws developed in the field and to their performance assessments, hence offering a fundamental tool for testing and development of WEC array models and their corresponding control strategies.

Annex: OCEAN open-access models

The open-access collection of models (which are described and validated in this work) named "*OCEAN — Open-access Collection of Experimental wave energy Arrays Nominal models*" is freely available at Pasta et al. (2024). The models are gathered inside the folder named 'models'. The files contained by this folder are:

- OCEAN_L0.mat: it contains the state-space matrices of the identified model of L0 layout.
- OCEAN_L1.mat: it contains the state-space matrices of the identified model of L1 layout.
- OCEAN_L2.mat: it contains the state-space matrices of the identified model of L2 layout.
- OCEAN_L3.mat: it contains the state-space matrices of the identified model of L3 layout.
- OCEAN_L4.mat: it contains the state-space matrices of the identified model of L4 layout.

Inside each of these files, the matrices A, B, and C (see (8)) of the identified (and validated) models are contained.

CRediT authorship contribution statement

Edoardo Pasta: Writing – review & editing, Writing – original draft, Visualization, Validation, Software, Methodology, Investigation, Funding acquisition, Formal analysis, Data curation, Conceptualization. **Guglielmo Papini:** Writing – review & editing, Visualization, Investigation, Data curation. **Yerai Peña-Sanchez:** Methodology, Investigation, Funding acquisition, Data curation. **Facundo D. Mosquera:** Visualization, Investigation. **Francesco Ferri:** Supervision, Resources, Project administration, Methodology, Investigation, Funding acquisition, Data curation. **Nicolás Faedo:** Writing – review & editing, Supervision, Resources, Project administration, Methodology, Funding acquisition, Formal analysis, Data curation.

Declaration of competing interest

The authors declare that they have no known competing financial interests or personal relationships that could have appeared to influence the work reported in this paper.

Acknowledgements

The authors are grateful with Dr. M. Folley, from Queen's University Belfast, for his valuable input during the execution of the experimental campaign. The support of Dr. S. Wood is also appreciated by the authors. This project has received funding from the European Union's Horizon 2020 research and innovation programme under the Marie Sklodowska-Curie grant agreements No 101024372, and No 101034297, and support from the framework COST Action 17105 - WECANet.

References

Anderlini, E., Forehand, D., Bannon, E., Xiao, Q., & Abusara, M. (2018). Reactive control of a two-body point absorber using reinforcement learning. *Ocean Engineering*, *148*, 650–658. http://dx.doi.org/10.1016/j.oceaneng.2017.08.017.

Anderlini, E., Forehand, D. I. M., Stansell, P., Xiao, Q., & Abusara, M. (2016). Control of a point absorber using reinforcement learning. *IEEE Transactions on Sustainable Energy*, *7*(4), 1681–1690. http://dx.doi.org/10.1109/TSTE.2016.2568754.

Astariz, S., & Iglesias, G. (2015). The economics of wave energy: A review. *Renewable and Sustainable Energy Reviews*, *45*, 397–408. http://dx.doi.org/10.1016/j.rser.2015.01.061.

Auger, C., Merigaud, A., & Ringwood, J. V. (2019). Receding-horizon pseudo-spectral control of wave energy converters using periodic basis functions. *IEEE Transactions on Sustainable Energy*, *10*(4), 1644–1652. http://dx.doi.org/10.1109/TSTE.2018.2868546.

Babarit, A., & Delhommeau, G. (2015). Theoretical and numerical aspects of the open source BEM solver NEMOH. In *11th European wave and tidal energy conference*.

Bacelli, G., & Ringwood, J. V. (2013). A geometric tool for the analysis of position and force constraints in wave energy converters. *Ocean Engineering*, *65*, 10–18. http://dx.doi.org/10.1016/j.oceaneng.2013.03.011.

Bracco, G., Canale, M., & Cerone, V. (2020). Optimizing energy production of an inertial sea wave energy converter via model predictive control. *Control Engineering Practice*, *96*, http://dx.doi.org/10.1016/j.conengprac.2020.104299.

Carapellese, F. (2023). *Dynamic design of a novel inertial reaction mass wave energy converter: The SWINGO device* (Ph.D. thesis), Italy: Politecnico di Torino.

Carapellese, F., Pasta, E., Paduano, B., Faedo, N., & Mattiazzo, G. (2022). Intuitive LTI energy-maximising control for multi-degree of freedom wave energy converters: The PeWEC case. *Ocean Engineering*, *256*, Article 111444. http://dx.doi.org/10.1016/j.oceaneng.2022.111444.

Carapellese, F., Pasta, E., Sirigu, S. A., & Faedo, N. (2023). SWINGO: Conceptualisation, modelling, and control of a swinging omnidirectional wave energy converter. *Mechanical Systems and Signal Processing*, *197*, Article 110356. http://dx.doi.org/10.1016/j.ymssp.2023.110356.

Centeno-Telleria, M., Aizpurua, J. I., & Penalba, M. (2022). An analytical model for a holistic and efficient O&M assessment of offshore renewable energy systems. *SSRN Electronic Journal*, http://dx.doi.org/10.2139/ssrn.4273477.

Chui, C. K., & Chen, G. (2017). *Kalman filtering*. Cham: Springer International Publishing, http://dx.doi.org/10.1007/978-3-319-47612-4.

Clément, A., McCullen, P., Falcão, A., Fiorentino, A., Gardner, F., Hammarlund, K., et al. (2002). Wave energy in Europe: current status and perspectives. *Renewable and Sustainable Energy Reviews*, *6*(5), 405–431. http://dx.doi.org/10.1016/S1364-0321(02)00009-6.

Coe, R. G., Bacelli, G., & Forbush, D. (2021). A practical approach to wave energy modeling and control. *Renewable and Sustainable Energy Reviews*, *142*, Article 110791. http://dx.doi.org/10.1016/j.rser.2021.110791.

Faedo, N., Carapellese, F., Pasta, E., & Mattiazzo, G. (2022). On the principle of impedance-matching for underactuated wave energy harvesting systems. *Applied Ocean Research*, *118*, Article 102958. http://dx.doi.org/10.1016/j.apor.2021.102958.

Faedo, N., Garcia-Violini, D., Peña-Sanchez, Y., & Ringwood, J. V. (2020). Optimisation-vs. non-optimisation-based energy-maximising control for wave energy converters: A case study. In *2020 European control conference* (pp. 843–848). IEEE, http://dx.doi.org/10.23919/ECC51009.2020.9143751.

Faedo, N., Mosquera, F. D., Pasta, E., Papini, G., Peña-Sanchez, Y., Evangelista, C. A., et al. (2024). Experimental assessment of combined sliding mode & moment-based control (SM2C) for arrays of wave energy conversion systems. *Control Engineering Practice*, *144*, Article 105818.

Faedo, N., Peña-Sanchez, Y., Garcia-Violini, D., Ferri, F., Mattiazzo, G., & Ringwood, J. V. (2023). Experimental assessment and validation of energy-maximising moment-based optimal control for a prototype wave energy converter. *Control Engineering Practice*, *133*, Article 105454. http://dx.doi.org/10.1016/j.conengprac.2023.105454.

Faedo, N., Peña-Sanchez, Y., Pasta, E., Papini, G., Mosquera, F. D., & Ferri, F. (2023). SWELL: An open-access experimental dataset for arrays of wave energy conversion systems. *Renewable Energy*, *212*, 699–716. http://dx.doi.org/10.1016/j.renene.2023.05.069.

Faedo, N., Peña-Sanchez, Y., & Ringwood, J. V. (2021). Receding-horizon energy-maximising optimal control of wave energy systems based on moments. *IEEE Transactions on Sustainable Energy*, *12*(1), 378–386. http://dx.doi.org/10.1109/TSTE.2020.3000013.

Faedo, N., Scarciotti, G., Astolfi, A., & Ringwood, J. V. (2018). Energy-maximising control of wave energy converters using a moment-domain representation. *Control Engineering Practice*, *81*, 85–96. http://dx.doi.org/10.1016/j.conengprac.2018.08.010.

Falcão, A. F. d. O. (2010). Wave energy utilization: A review of the technologies. *Renewable and Sustainable Energy Reviews*, *14*(3), 899–918. http://dx.doi.org/10.1016/j.rser.2009.11.003.

Farajvand, M., Garcia-Violini, D., Windt, C., Grazioso, V., & Ringwood, J. V. (2021). Quantifying hydrodynamic model uncertainty for robust control of wave energy devices. In *European wave and tidal energy conference series, Proceedings of the 14th European wave and tidal energy conference* (pp. 2251–1–2251–10). Plymouth, UK.

Folley, M. (2016). *Numerical modelling of wave energy converters: state-of-the-art techniques for single devices and arrays*. Elsevier, http://dx.doi.org/10.1016/C2014-0-04006-3.

Garcia-Rosa, P. B., Bacelli, G., & Ringwood, J. V. (2015). Control-informed optimal array layout for wave farms. *IEEE Transactions on Sustainable Energy*, *6*(2), 575–582. http://dx.doi.org/10.1109/TSTE.2015.2394750.

Garcia-Violini, D., Peña-Sanchez, Y., Faedo, N., & Ringwood, J. V. (2020). An energy-maximising Linear Time Invariant Controller (LiTe-Con) for wave energy devices. *IEEE Transactions on Sustainable Energy*, *11*(4), 2713–2721. http://dx.doi.org/10.1109/TSTE.2020.2971392.

Garcia-Violini, D., Peña-Sanchez, Y., Faedo, N., Windt, C., Ferri, F., & Ringwood, J. V. (2021). Experimental implementation and validation of a broadband LTI energy-maximizing control strategy for the wavestar device. *IEEE Transactions on Control Systems Technology*, *29*(6), 2609–2621. http://dx.doi.org/10.1109/TCST.2021.3052479.

Guanche, R., de Andrés, A., Losada, I., & Vidal, C. (2015). A global analysis of the operation and maintenance role on the placing of wave energy farms. *Energy Conversion and Management*, *106*, 440–456. http://dx.doi.org/10.1016/j.enconman.2015.09.022.

Guo, B., & Ringwood, J. V. (2021). A review of wave energy technology from a research and commercial perspective. *IET Renewable Power Generation*, *15*(14), 3065–3090. http://dx.doi.org/10.1049/rpg2.12302.

Hansen, R. H., & Kramer, M. M. (2011). Modelling and control of the wavestar prototype. In *Proceedings of the 9th European wave and tidal energy conference* (p. 10).

Hasselmann, K., Barnett, T. P., Bouws, E., Carlson, H., Cartwright, D. E., Enke, K., et al. (1973). Measurements of wind-wave growth and swell decay during the joint north sea wave project (JONSWAP). *Ergänzungsheft zur Deutschen Hydrographischen Zeitschrift, Reihe A*, *12*.

Hosseini, S. E. (2020). An outlook on the global development of renewable and sustainable energy at the time of COVID-19. *Energy Research & Social Science*, *68*, Article 101633. http://dx.doi.org/10.1016/j.erss.2020.101633.

Jama, M., Wahyudie, A., & Noura, H. (2018). Robust predictive control for heaving wave energy converters. *Control Engineering Practice*, *77*, 138–149. http://dx.doi.org/10.1016/j.conengprac.2018.05.010.

Li, G., & Belmont, M. R. (2014). Model predictive control of sea wave energy converters – Part II: The case of an array of devices. *Renewable Energy*, *68*, 540–549. http://dx.doi.org/10.1016/j.renene.2014.02.028.

Li, N., García-Medina, G., Cheung, K. F., & Yang, Z. (2021). Wave energy resources assessment for the multi-modal sea state of Hawaii. *Renewable Energy*, *174*, 1036–1055. http://dx.doi.org/10.1016/j.renene.2021.03.116.

Ljung, L. (1999). *System identification: Theory for the user* (2nd ed.). (p. 609). Prentice Hall PTR.

Mareels, I. (1984). Sufficiency of excitation. *Systems & Control Letters*, *5*(3), 159–163. http://dx.doi.org/10.1016/S0167-6911(84)80097-3.

McKelvey, T., Akcay, H., & Ljung, L. (1996). Subspace-based multivariable system identification from frequency response data. *IEEE Transactions on Automatic Control*, *41*(7), 960–979. http://dx.doi.org/10.1109/9.508900.

Mérigaud, A., & Ringwood, J. V. (2016). Condition-based maintenance methods for marine renewable energy. *Renewable and Sustainable Energy Reviews*, *66*, 53–78. http://dx.doi.org/10.1016/j.rser.2016.07.071.

Mérigaud, A., & Ringwood, J. V. (2018). Towards realistic non-linear receding-horizon spectral control of wave energy converters. *Control Engineering Practice*, *81*, 145–161. http://dx.doi.org/10.1016/j.conengprac.2018.08.024.

Moens de Hase, D., Pasta, E., Faedo, N., & Ringwood, J. V. (2021). Towards efficient extremum-seeking control of wave energy systems: possibilities and pitfalls. In *14th European wave and tidal energy conference*.

Mork, G., Barstow, S., Kabuth, A., & Pontes, M. T. (2010). Assessing the global wave energy potential. In *29th international conference on ocean, offshore and arctic engineering*: *vol. 3*, (pp. 447–454). ASMEDC, http://dx.doi.org/10.1115/OMAE2010-20473.

Nastasi, B., Markovska, N., Puksec, T., Duić, N., & Foley, A. (2022). Renewable and sustainable energy challenges to face for the achievement of sustainable development goals. *Renewable and Sustainable Energy Reviews*, *157*, Article 112071. http://dx.doi.org/10.1016/j.rser.2022.112071.

Nguyen, H. N., & Tona, P. (2018). Short-term wave force prediction for wave energy converter control. *Control Engineering Practice*, *75*, 26–37. http://dx.doi.org/10.1016/j.conengprac.2018.03.007.

O'Sullivan, A. C. M., Sheng, W., & Lightbody, G. (2018). An analysis of the potential benefits of centralised predictive control for optimal electrical power generation from wave energy arrays. *IEEE Transactions on Sustainable Energy*, *9*(4), 1761–1771. http://dx.doi.org/10.1109/TSTE.2018.2812749.

Parrinello, L., Dafnakis, P., Pasta, E., Bracco, G., Naseradinmousavi, P., Mattiazzo, G., et al. (2020). An adaptive and energy-maximizing control optimization of wave energy converters using an extremum-seeking approach. *Physics of Fluids*, *32*(11), Article 113307. http://dx.doi.org/10.1063/5.0028500.

Pasta, E., Faedo, N., Mattiazzo, G., & Ringwood, J. V. (2023). Towards data-driven and data-based control of wave energy systems: Classification, overview, and critical assessment. *Renewable and Sustainable Energy Reviews*, *188*, Article 113877. http://dx.doi.org/10.1016/j.rser.2023.113877.

Pasta, E., Paduano, B., Mattiazzo, G., Faedo, N., & Ringwood, J. V. (2023). On data-based control-oriented modelling applications in wave energy systems. In *Proceedings of the 15th European wave and tidal energy conference* (p. 409). Bilbao, Spain: http://dx.doi.org/10.36688/ewtec-2023-409.

Pasta, E., Papini, G., Faedo, N., Mattiazzo, G., & Ringwood, J. (2022). On optimization-based strategies in data-driven control of wave energy systems. In *Trends in renewable energies offshore* (pp. 401–409). London: CRC Press, http://dx.doi.org/10.1201/9781003360773-46.

Pasta, E., Papini, G., Pena-Sanchez, Y., Mosquera, F. D., Ferri, F., & Faedo, N. (2024). OCEAN - Open-access validated models from experimental data of wave energy system arrays. http://dx.doi.org/10.17632/97cpczdg2r.1.

Peña-Sanchez, Y., Merigaud, A., & Ringwood, J. V. (2020). Short-term forecasting of sea surface elevation for wave energy applications: The autoregressive model revisited. *IEEE Journal of Oceanic Engineering*, *45*(2), 462–471. http://dx.doi.org/10.1109/JOE.2018.2875575.

Peña-Sanchez, Y., Windt, C., Davidson, J., & Ringwood, J. V. (2020). A critical comparison of excitation force estimators for wave-energy devices. *IEEE Transactions on Control Systems Technology*, *28*(6), 2263–2275. http://dx.doi.org/10.1109/TCST.2019.2939092.

Penalba, M., & Ringwood, J. V. (2019). A high-fidelity wave-to-wire model for wave energy converters. *Renewable Energy*, *134*, 367–378. http://dx.doi.org/10.1016/j.renene.2018.11.040.

Pierson, W. J., & Moskowitz, L. (1964). A proposed spectral form for fully developed wind seas based on the similarity theory of S. A. Kitaigorodskii. *Journal of Geophysical Research*, *69*(24), 5181–5190. http://dx.doi.org/10.1029/JZ069i024p05181.

Ringwood, J. V. (2020). Wave energy control: status and perspectives 2020. *IFAC-PapersOnLine*, *53*(2), 12271–12282. http://dx.doi.org/10.1016/j.ifacol.2020.12.1162.

Ringwood, J. V., Bacelli, G., & Fusco, F. (2014). Energy-maximizing control of wave-energy converters: The development of control system technology to optimize their operation. *IEEE Control Systems*, *34*(5), 30–55. http://dx.doi.org/10.1109/MCS.2014.2333253.

Ringwood, J., Ferri, F., Tom, N., Ruehl, K., Faedo, N., Bacelli, G., et al. (2019). The wave energy converter control competition: Overview. In *Ocean renewable energy*: *vol. 10*, American Society of Mechanical Engineers, http://dx.doi.org/10.1115/OMAE2019-95216.

Ringwood, J. V., Zhan, S., & Faedo, N. (2023). Empowering wave energy with control technology: Possibilities and pitfalls. *Annual Reviews in Control*, http://dx.doi.org/10.1016/j.arcontrol.2023.04.004.

Rosati, M., Said, H. A., & Ringwood, J. V. (2023). Wave-to-wire control of an oscillating water column wave energy system equipped with a wells turbine. In *Proceedings of the 15th European wave and tidal energy conference*. Bilbao.

Said, H. A., García-Violini, D., & Ringwood, J. V. (2022). Wave-to-grid (W2G) control of a wave energy converter. *Energy Conversion and Management: X*, *14*, Article 100190. http://dx.doi.org/10.1016/j.ecmx.2022.100190.

Said, H., & Ringwood, J. (2022). Low voltage ride-through capability enhancement of a grid-connected wave energy conversion system. In *Trends in renewable energies offshore* (pp. 267–275). http://dx.doi.org/10.1201/9781003360773-31.

Scavalla, A., Rossi, A., La Battaglia, V., & Pio Belfiore, N. (2023). A survey of wave energy converter mechanisms presented under the topological and functional viewpoints. *Journal of Mechanical Design*, *145*(7), http://dx.doi.org/10.1115/1.4057057.

Schoukens, J., & Ljung, L. (2019). Nonlinear system identification: A user-oriented road map. *IEEE Control Systems*, *39*(6), 28–99. http://dx.doi.org/10.1109/MCS.2019.2938121.

Scruggs, J., Lattanzio, S., Taflanidis, A., & Cassidy, I. (2013). Optimal causal control of a wave energy converter in a random sea. *Applied Ocean Research*, *42*, 1–15. http://dx.doi.org/10.1016/j.apor.2013.03.004.

Scruggs, J., & Nie, R. (2015). Disturbance-adaptive stochastic optimal control of energy harvesters, with application to ocean wave energy conversion. *Annual Reviews in Control*, *40*, 102–115. http://dx.doi.org/10.1016/j.arcontrol.2015.09.017.

Ströfer, C. A. M., Gaebele, D. T., Coe, R. G., & Bacelli, G. (2023). Control co-design of power take-off systems for wave energy converters using WecOptTool. *IEEE Transactions on Sustainable Energy*, 1–11. http://dx.doi.org/10.1109/TSTE.2023.3272868.

Tona, P., Sabiron, G., Nguyen, H. N., Mérigaud, A., & Ngo, C. (2020). Experimental assessment of the IFPEN solution to the WEC control competition. In *Ocean renewable energy*: *vol. 9*, American Society of Mechanical Engineers, http://dx.doi.org/10.1115/OMAE2020-18669.

Trueworthy, A., & DuPont, B. (2020). The wave energy converter design process: Methods applied in industry and shortcomings of current practices. *Journal of Marine Science and Engineering*, *8*(11), 932. http://dx.doi.org/10.3390/jmse8110932.

Vázquez y Torres Ingeniería SL. (VTI) (2024). VTI wavemakers. URL: https://www.vtisl.com/en/test-systems/wave-laboratories/.

Vining, J. G., & Muetze, A. (2007). Governmental regulation of ocean wave energy converter installations. In *2007 IEEE industry applications annual meeting* (pp. 749–755). IEEE, http://dx.doi.org/10.1109/07IAS.2007.118.

Willems, J. C., Rapisarda, P., Markovsky, I., & De Moor, B. L. (2005). A note on persistency of excitation. *Systems & Control Letters*, *54*(4), 325–329. http://dx.doi.org/10.1016/j.sysconle.2004.09.003.

Windt, C., Faedo, N., Penalba, M., Dias, F., & Ringwood, J. V. (2021). Reactive control of wave energy devices – the modelling paradox. *Applied Ocean Research*, *109*, Article 102574. http://dx.doi.org/10.1016/j.apor.2021.102574.

Zhan, S., Li, G., Na, J., & He, W. (2019). Feedback noncausal model predictive control of wave energy converters. *Control Engineering Practice*, *85*, 110–120. http://dx.doi.org/10.1016/j.conengprac.2018.12.015.

Zurkinden, A., Ferri, F., Beatty, S., Kofoed, J., & Kramer, M. (2014). Non-linear numerical modeling and experimental testing of a point absorber wave energy converter. *Ocean Engineering*, *78*, 11–21. http://dx.doi.org/10.1016/j.oceaneng.2013.12.009.